

PAPER • OPEN ACCESS

Planar laser-induced fluorescence system for spatiotemporal ion velocity distribution function measurements

To cite this article: S H Son et al 2025 Plasma Sources Sci. Technol. 34 105003

View the <u>article online</u> for updates and enhancements.

You may also like

- Simulation study of mode transitions induced by external control parameters in capacitively coupled oxygen discharges Chong-Biao Tian, Li Wang, Máté Vass et al.
- Control of the chemistry of a humidified He RF atmospheric pressure plasma jet by pulse modulation Steffen Schüttler, Maike Kai, Emanuel Jeß et al
- Electrical charge decay on dielectric surface in nitrogen/C₄F₇N mixtures
 D Prokop, M Mrkviková, J Tungli et al.

Plasma Sources Sci. Technol. 34 (2025) 105003 (18pp)

Planar laser-induced fluorescence system for spatiotemporal ion velocity distribution function measurements

S H Son^{1,2,*}, I Romadanov², N S Chopra^{1,2} and Y Raitses²

E-mail: sson2@pppl.gov

Received 22 April 2025, revised 4 August 2025 Accepted for publication 19 September 2025 Published 6 October 2025



Abstract

In this work, we present a planar laser-induced fluorescence (PLIF) system for measuring two-dimensional (2D), spatiotemporally resolved ion velocity distribution functions (IVDFs). A continuous-wave tunable diode laser produces a laser sheet that irradiates the plasma, and the resulting fluorescence is captured by an intensified CCD (ICCD) camera. Fluorescence images recorded at varying laser wavelengths are converted into 2D IVDFs using the Doppler shift principle. The developed diagnostic is implemented in an electron beam generated $E \times B$ plasma with a bulk plasma density of $\sim 10^{10} \text{cm}^{-3}$. The developed diagnostic is validated against a conventional single-point LIF method using photomultiplier tube-based detection, while significantly reducing the total measurement time by the number of spatial positions measured. The time-resolving capability of this diagnostic is tested by oscillating the plasma between two nominal operating modes with different density profiles and triggering the ICCD camera by the externally driven plasma oscillation. The measured 2D IVDF maps reveal several signatures of ion dynamics in this plasma source, including radially outflowing ions across the electric field and anomalous ion heating at the periphery, consistent with recent kinetic simulations and theoretical studies. A possible correlation between these ion kinetic features and rotating spoke structures is discussed.

Keywords: planar laser-induced fluorescence (PLIF), ion velocity distribution function (IVDF), $E \times B$ plasma, electron beam generated plasma, rotating spoke, ion heating, partially magnetized

1. Introduction

Spatially resolved measurements of the ion velocity distribution function (IVDF) can be critical for low-temperature plasmas and their applications as they provide detailed

Original content from this work may be used under the terms of the Creative Commons Attribution 4.0 licence. Any further distribution of this work must maintain attribution to the author(s) and the title of the work, journal citation and DOI.

insights into transport, sheath dynamics, and other fundamental plasma processes [1–6]. Recently, the demand for temporally resolved measurements has also increased, in response to advances in modern plasma sources that exhibit various time-dependent characteristics of ion dynamics [7–11]. For example, $E \times B$ plasmas, including Hall thrusters, Penning discharges, and magnetic nozzles, feature various instabilities that may lead to anomalous transport and heating of ions [12–18]. Additionally, processing plasmas such as capacitively coupled plasmas and inductively coupled plasmas are frequently operated in pulsed modes [19–23] or driven by arbitrary bias waveforms [24–26], resulting in IVDFs that evolve over time. Therefore, diagnostics capable of resolving

¹ Department of Astrophysical Sciences, Princeton University, Princeton, NJ, United States of America

² Princeton Plasma Physics Laboratory, Princeton, NJ, United States of America

^{*} Author to whom any correspondence should be addressed.

IVDFs in both space and phase are of broad interest for understanding and improving modern plasma sources.

Laser-induced fluorescence (LIF) is a widely used, noninvasive diagnostic technique for studying ion and neutral dynamics in various low-temperature plasma sources [27–31]. In this method, a laser optically pumps the ions and/or neutrals in the plasma, and the resulting fluorescence emission is analyzed. By sweeping the laser wavelength across an absorption line of a target ion species, either in a ground or metastable state, IVDFs can be measured using the Doppler shift principle. Ions with velocity v along the laser wavevector perceive a Doppler-shifted laser frequency $\Delta f = v/\lambda_0$, where λ_0 is the laser wavelength in the laboratory frame. Consequently, only ions with a velocity component matching the laser frequency are resonantly excited. By mapping fluorescence intensity as a function of laser wavelength, the IVDF can be reconstructed. Since ground-state excitation typically requires higher-energy lasers, transitions from long-lived metastable states are often used in practice. In such cases, it is generally assumed that the metastable ion population is in thermal equilibrium with the bulk ion population, allowing the reconstructed IVDF to represent the overall ion dynamics [29].

In practice, conventional LIF diagnostics involve directing a focused laser beam into the plasma and collecting the resulting fluorescence at a single point (0D) using a photodetector, such as a photomultiplier tube (PMT). For spatially resolved measurements, spatial scans can be performed by mounting the laser beam, the fluorescence collection optics [28], or the plasma source itself [32] on translational stages. However, this scanning approach is inherently slow, as it requires a full laser wavelength sweep at each spatial position. Consequently, the total measurement time becomes N times longer than a singlepoint measurement, where N is the number of spatial positions of interest. Additionally, this approach limits each spatial point to be recorded at a different time, making it unsuitable for plasma sources that drift or evolve, even over relatively long timescales on the order of minutes or hours. For example, plasmas generated by thermionically emitting cathodes, which exhibit thermal drift [33], various processing plasmas that experience drift due to material sputtering and evolving wall conditions [34], or Hall thrusters during transitional operation period [35], require alternatives to conventional LIF systems.

To overcome the limitations of point-by-point LIF scanning, planar LIF (PLIF) techniques could be considered. In PLIF, a laser sheet illuminates a broad region of the plasma, and a camera with a wide field of view (FOV) captures a two-dimensional (2D) fluorescence map in a single acquisition, eliminating the need for mechanical spatial scanning. However, expanding the laser beam into a sheet inherently reduces its intensity, leading to weaker fluorescence signals. This, when combined with quenching of the excited metastable, often results in signals falling below detection limits [36]. High-power pulsed lasers have been used to compensate this, but their broad linewidths limit the velocity resolution of the measured IVDFs [7, 37–40].

Despite their limitations in power, continuous-wave (CW) lasers offer a compelling advantage in velocity resolution due to their much narrower linewidths. However, their relatively low intensity has hindered widespread application in PLIF systems, which require sufficient signal strength for 2D imaging. In conventional LIF setups, weak fluorescence induced by CW lasers is often recovered using lock-in amplification, a technique that enhances signal-to-noise ratio by modulating the laser and synchronizing detection [27–31]. However, in imaging-based diagnostics, low signal levels often require extended camera times to accumulate sufficient photons, making temporally resolved detection impractical. Consequently, lock-in amplification cannot be directly applied to most PLIF systems targeting low-density plasmas. Under these conditions, alternative approaches such as image denoising become essential.

As a result, the use of CW lasers in PLIF or camerabased LIF systems remains limited, and only a few studies have reported such applications for IVDF measurements. Lee et al [41] measured time-averaged 1D IVDFs in the sheath of a filament-discharge plasma using a low-power (~15 mW) CW tunable diode laser (TDL) and an intensified CCD (ICCD) camera for detection. However, the reduced intensity of the expanded laser sheet was insufficient for diagnosing 2D maps of IVDFs. Paul and Scime [42] reported the first 2D-resolved IVDFs using a tunable CW dye laser (~70 mW) shaped into a laser sheet and a fast-frame camera detection. This work was conducted on the PHASMA (Phase Space Mapping) experiment [43] with plasma densities on the order of $10^{12} - 10^{13} \text{cm}^{-3}$, which is several hundred to thousand times denser than typical sheath or bulk plasma densities encountered in industrial plasma sources [9, 44, 45]. In summary, despite recent advances, the applicability of PLIF for resolving 2D IVDFs in various low- to moderate-density lowtemperature plasmas has not yet been demonstrated, either for time-averaged and time-resolved measurements.

In this paper, we present the development of a PLIF system utilizing a compact, low-power (\sim 20 mW) CW TDL for the laser-induced excitation of metastables and an ICCD camera for the fluorescence detection. The use of a TDL in place of a dye laser provides a cost-effective and convenient alternative, while eliminating chemical hazards and reducing the space requirements associated with large dye-laser systems. The system is implemented in an electron beam generated $E \times B$ plasma with a moderate bulk plasma density \sim 10¹⁰cm⁻³, which is a regime more representative of industrial plasma applications. Using this setup, we demonstrate 2D, time-resolved measurements of IVDFs, and discuss key features of ion dynamics revealed through this PLIF system.

This paper is organized as follows:

Section 2 introduces the experimental setup, including the target plasma source used as a test bench. Section 3 provides details on the development of the PLIF system, showing optical components, the operating scheme, and a quantitative analysis of image denoising methods. Section 4 presents

the validation of time-averaged and time-resolved 2D IVDF measurements. Section 5 casts discussions on the observed ion dynamics, in comparison to recent theoretical and modeling studies. Conclusion is provided in section 6.

2. Experimental setup

An electron beam generated $E \times B$ plasma source is used as a test bench for the developed diagnostics. A schematic of the plasma source is shown in figure 1(a).

This plasma source consists of a cylindrical vacuum chamber with a radius of $r_{\rm ch} = 10 {\rm cm}$ and length of $L_{\rm ch} = 50 {\rm cm}$, which is pumped down to a base pressure of 1μ Torr using a turbo-molecular pump backed by a roughing pump. A leak valve placed between the gas cylinder and the vacuum change is used to fill the chamber with argon gas and regulate the background pressure in the range of 0.1 - 0.5 mTorr. An axial (z-direction) magnetic field of $50 - 100 \,\mathrm{G}$ is generated by a Helmholtz-like coil along the chamber. Electrons are thermionically emitted from a tungsten filament and accelerated across the cathode sheath in front of a stainless-steel plate with a radius of $r_c = 4.5$ cm, located at one end of the chamber. The cathode and cathode plate are biased to a negative DC potential of $V_{\rm c} = -55$ V relative to the grounded chamber. The electron beam is guided by the axial magnetic field, and a portion of the beam collides with neutral argon atoms, initiating a cylindrical plasma discharge. A laser sheet is aligned in the (r-z)plane of this plasma, as indicated by a red transparent box. In addition to the cathode plate, an electrically isolated, nonmagnetic stainless-steel plate, referred to as the anticathode, with a radius of $r_{\rm atc} = 4.5$ cm is installed at the end of the chamber opposite the cathode. The chamber is equipped with various electrostatic probes that measure the radial profiles of plasma parameters, including a Langmuir probe (LP) to measure electron energy distribution function (EEDF), floating emissive probe (EP) to measure plasma potential, and ion probe (IP) to measure time-evolution of ion density under thick sheath assumption. More details on the electrostatic diagnostics can be found in [47].

We have investigated various characteristics of this plasma source under different operating conditions. For example, ion kinetics such as warm-ion production [48], electron kinetics [49], and instabilities such as rotating spokes [10] have been observed. Notably, by varying the voltage applied to the anticathode plate, the plasma can operate in one of two distinct modes-collector mode and repeller mode-as identified in our previous work [49]. In the collector mode, the anticathode is grounded ($V_{atc} = 0 \text{ V}$), allowing it to collect nearly all incident electrons. In contrast, in the repeller mode, the anticathode is biased to the cathode potential or lower ($V_{\rm atc} \leq V_{\rm c}$), repelling plasma and beam electrons back into the plasma volume. Consequently, repeller mode produces a higher plasma density compared to the collector mode. This clear mode transition is particularly useful for evaluating the time-resolving capability of the diagnostic system.

To evaluate the performance of the developed LIF system, this source is used as a test bench under two distinct operating scenarios, A and B, corresponding to (A) time-averaged and (B) time-resolved measurements of spatially resolved IVDFs. The operating parameters for each case are summarized in table 1. The radial profile of plasma parameters for scenario (A) is provided in [47, 49], and that for scenario (B) is presented in section 4.2. In the electron-beam region, highlighted in yellow, spanning from the center to r = 10 mm, the EEDF exhibits a larger high-energy population due to the beam propagating along the axial direction [49]. As a result, the electron temperature profile is radially non-uniform, with higher effective temperatures at the center and lower values toward the periphery (r = 20 mm), reflecting the characteristics of the electron-beam-generated plasma source. This enhanced high-energy tail increases the excitation efficiency of ion metastable states near the core.

In scenario (A), the anticathode is biased to a constant DC voltage of $V_{\text{atc}} = -55 \text{ V}$. So, the plasma stays in the repeller mode. Note that a prominent azimuthal structure, the so-called rotating spoke, exists in the plasma bulk. In scenario (B), the anticathode is AC-modulated as $V_{\text{atc}} = V_0 (1 + \sin(2\pi f t))$, where $V_0 = -37$ V and f = 0.5 kHz. This modulation causes the plasma to oscillate slowly between collector and the repeller modes with an oscillation period $\tau = 2$ ms, resulting in periodic fluctuations in plasma density. Time-resolved PLIF is employed to capture the corresponding variation in the fluorescence profiles associated with this density modulation. Note that the use of higher pressure and a weaker magnetic field in scenario (B) significantly suppresses the rotating spoke, making the collector-to-repeller mode transition the most prominent temporal feature. This behavior is beneficial for diagnostic triggering, and it will be discussed further in the following section.

3. Diagnostics development

3.1. Optical setup

This section outlines the mechanical setup of the optical system used for diagnostics development. A schematic of the PLIF system developed in this study is presented in figure 2(a).

The system is built around a TDL, specifically a single-mode TOptica DLC DL PRO 670, which features a Littrow-type grating-stabilized external cavity design. This laser provides a coarse tuning range from 660 to 673 nm and a mode-hop-free tuning range of approximately 20 GHz. The output power is wavelength-dependent, with a maximum of approximately 23 mW. The laser wavelength is controlled by scanning the voltage applied to the laser's piezo actuator. A portion of the laser beam is sampled by a beam splitter (BS) and directed to a wavemeter (Bristol, 621-A), which features built-in continuous calibration using a single-frequency He–Ne laser and a specified accuracy of \pm 0.0002 nm at 1000 nm. The wavemeter's reading accuracy exceeds the TDL's linewidth, which limits the achievable

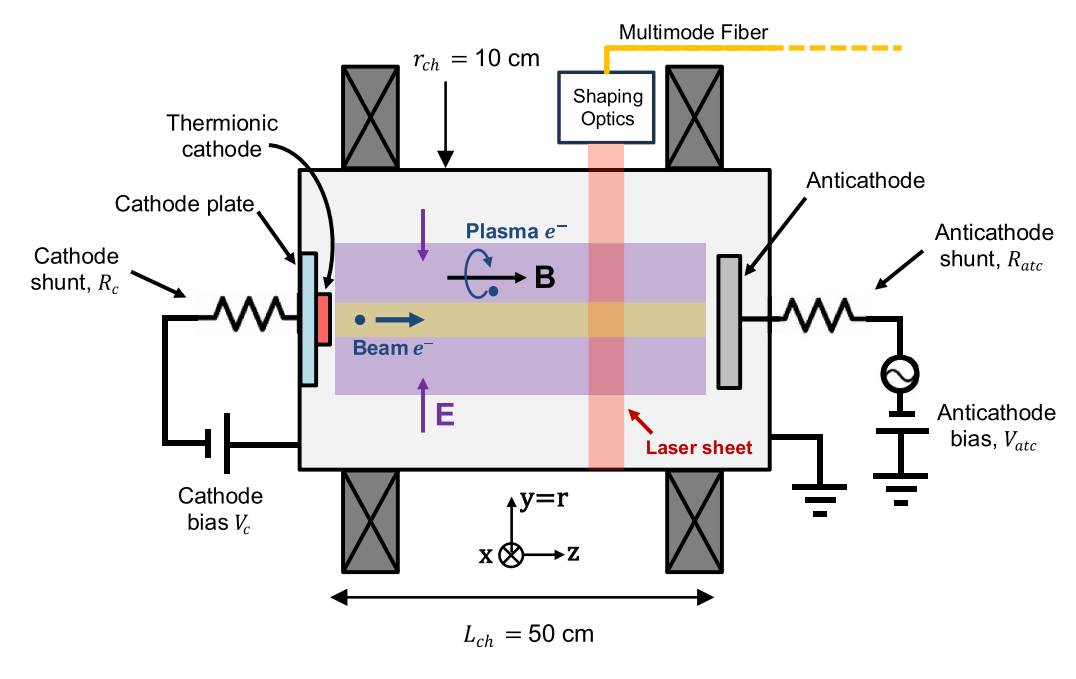


Figure 1. Schematic of the electron beam generated $E \times B$ plasma source. See [10, 46–50] for details.

Table 1. Experimental condition of each operating scenarios, (A) for time-averaged measurements, and (B) for time-resolved measurements. p: pressure, V_c : cathode voltage, V_{atc} : anticathode voltage or waveform, B_z : axial magnetic field intensity, n_p : plasma density measured at radial center, $T_{c,0}$: effective electron temperature at radial periphery (r = 2cm).

	Scenario (A) for time-averaged	Scenario (B) for time-resolved
p [mT]	0.1	0.5
V_c $[V]$		-55
V_{atc} [V]	-55	$V_0\left(1+\sin\left(2\pi ft\right)\right)$,
		$V_0 = -37 \text{ V},$
		f = 0.5 kHz
$B_z[G]$	100	50
$n_p \left[10^{10} \ cm^{-3} \right]$	2.5	2.5 - 4 (upon modulation)
$T_{e, 0}$ [eV]	~12	~5
$T_{e, 2}$ $[eV]$	~3	~1.8

velocity resolution to approximately $\Delta v = 89 \text{ m s}^{-1}$, as estimated from the Doppler shift principle. The corresponding resolution of the broadening, i.e. ion temperature is $\frac{1}{2}M_i(2\Delta v)^2 = 0.007 \text{ eV}$, where M_i is the mass of argon.

Various transition schemes are known for argon ion metastable states [27, 51], but careful selection is necessary, as the metastable population can vary depending on the characteristics of the electron energy distribution or metastable quenching effects [36]. In this work, we used the three-level transition involving the $3\text{d4F}^{7/2} - 4\text{p4D}^{5/2}$ states, with excitation at 668.6138 nm and fluorescence emission at 442.724 nm (both in vacuum). The $4\text{p4}D^{7/2}-3\text{d4F}^{9/2}$ transition, centered at 664.553 nm was also considered, but the chosen transition yielded higher fluorescence intensity. The laser wavelength is scanned around the central wavelength, $\lambda_0 = 668.6138$ nm.

For time-averaged PLIF measurements (section 4.1), the laser beam is modulated using a mechanical chopper to maintain consistency with a conventional LIF setup [48], ensuring proper validation of the developed system. For timeresolved measurements (section 4.2), the mechanical chopper is removed from the setup for operational convenience. The laser beam is delivered to the chamber via a fiber coupler and a multimode fiber. Upon exiting the fiber, the beam enters the shaping optics, which include a large area beam collimator that produces a circular Gaussian beam of approximately 12 mm diameter. Two parallel razor blades are used to trim the beam edges and shape it into a semi-planar laser sheet with a maximum power of 20 mW. The resulting laser sheet is approximately 12 mm wide and 1 mm thick. Note that a set of cylindrical lenses could also be used for beam shaping. The laser sheet is aligned to propagate in the (r-z) plane in the downward z

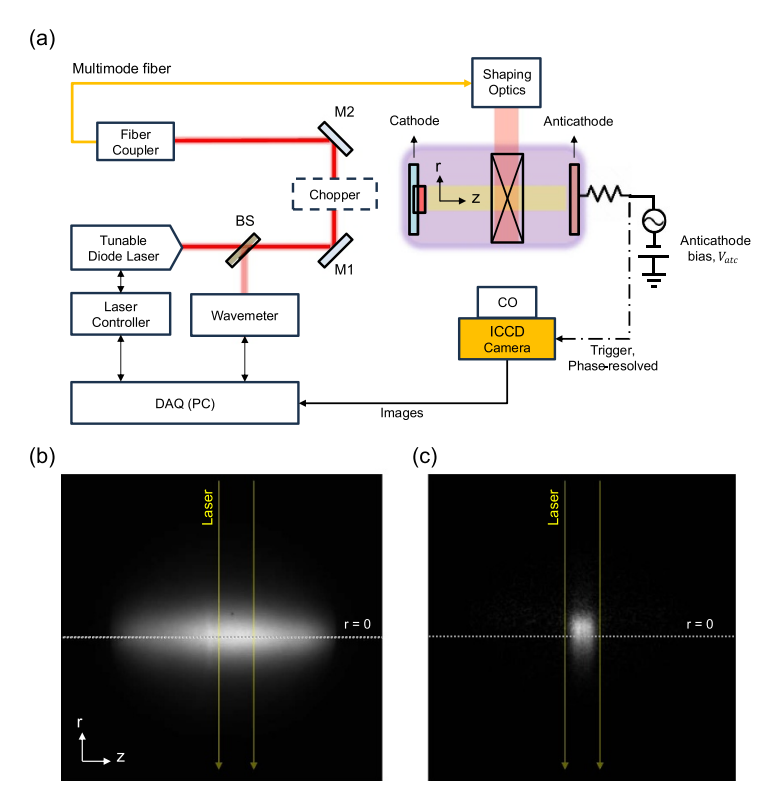


Figure 2. Schematic of the developed PLIF system. (a) Optical setup of the diagnostic system. The purple region indicates the plasma, and the black box with a cross mark indicates the region where laser-induced fluorescence is produced. Optical components are labeled as follows: BS—beam splitter; M—mirror; CO—collection optics. (b) Emission pattern captured using a PI-MAX 4:1024i camera. (c) Fluorescence pattern extracted by subtracting the background from (b). The plasma is operated under scenario (A), with the laser tuned to the central wavelength $\lambda_0 = 668.6138$ nm, within the wavemeter's uncertainty of $\Delta\lambda = \pm 0.0002$ nm. The direction and edge of the incident laser sheet are indicated by yellow arrows. Both images are normalized to their respective maximum intensities for visualization.

direction, enabling Doppler shifts due to the radial motion of the metastable argon ions.

The collection branch consists of a set of lens objectives, defining a FOV of $15 \text{ cm} \times 15 \text{ cm}$. A 441.6 nm/3 nm bandpass filter (Andover 442FS03-12.5) is installed in front of an ICCD camera (PI-MAX 4:1024i) as part of the collection optics. Details regarding the operating parameters of the ICCD camera are described in section 3.2.

Figure 2(b) shows an image acquired from the collection system with the laser tuned to the central wavelength λ_0 . Since the commercial bandpass filter used has a relatively broad bandwidth, it cannot fully eliminate stray light such as spontaneous plasma emission. As a result, the recorded fluorescence pattern is buried under background signals. To extract the fluorescence pattern, a background image, captured with the laser blocked from entering the plasma, is subtracted from the raw image. An example of the resulting fluorescence pattern is shown in figure 2(c). This procedure assumes that the background plasma emission remains sufficiently stable over time, such that its drift or fluctuation is smaller than the LIF during the wavelength scan. While this assumption can be important for plasmas that experience drift over the measurement timescale, it is less restrictive than for the PMTbased spatial scan, which requires plasma repeatability over the entire measurement period; otherwise, measurements at different positions may correspond to different plasma states. Since the ICCD-based system significantly reduces the total measurement time across multiple spatial positions, it is more tolerant of plasma drifts. Further discussion on this assumption can be found on the appendix A.

For time-averaged measurements, the fluorescence extraction procedure described above was repeated while tuning the laser wavelength around the central value of $\lambda_0 = 668.6138$ nm. Each pixel in the recorded images corresponds to a fluorescence intensity at a specific spatial location within the FOV. By applying the Doppler shift principle, IVDFs can be evaluated at each pixel, resulting in spatially resolved IVDFs.

For time-resolved measurements, the same procedure is applied, however, the timing of ICCD imaging is synchronized with the anticathode bias voltage. The oscillating voltage signal, branched from the anticathode, is fed into the device's built-in microchannel plate (MCP) triggering circuit, enabling image acquisition at specific phase intervals of the plasma oscillation. The ICCD camera is triggered during the collector and the repeller mode, with an exposure time set to one-tenth of the oscillation period ($\tau/10$), to demonstrate time-resolved LIF measurements of spatially resolved IVDFs. The temporal resolution of this PLIF system is governed by the ICCD camera's gate width (i.e. exposure time), which must be adjusted based on the fluorescence intensity emitted from the plasma. The ICCD camera used in this study offers multiple gating

Table 2. Measurement uncertainties of PMT-based and ICCD-based PLIF system.

	PMT-based LIF system	ICCD-based PLIF system	
Position uncertainty	$\pm 2.5~\mathrm{mm}$	$\pm 0.435~\mathrm{mm}$	
Spatial resolution	$\pm 0.9~\mathrm{mm}$	$\pm 0.435~\mathrm{mm}$	
Velocity uncertainty	$\pm 89 \text{ m s}^{-1}$		
Temperature uncertainty	0.007 eV		

options, including MCP gating, with gate widths as short as <8 ns. It should be noted, however, that this nanosecond-scale gating capability does not inherently guarantee nanosecond temporal resolution for all PLIF experiments across different plasma conditions. In low-density plasmas, where fluorescence signals are weak, both the gate width and achievable temporal resolution must be increased accordingly. The time resolution of conventional PMT-based LIF diagnostics requires more rigorous treatment depending on the optical setups, as discussed in [52].

The spatial resolution and positional uncertainty of the measured IVDFs are governed by the physical area on the FOV corresponding to a single CCD pixel. Considering the magnification of the lens objectives and the pixel size of the ICCD camera used in our system, each pixel collects fluorescence from a square region of $\Delta L \times \Delta L = 0.145$ mm $\times 0.145$ mm in the (r-z) focal plane. To suppress speckle noise caused by dark current or cosmic rays, fluorescence at each pixel is averaged with its surrounding square neighborhood, yielding an effective spatial resolution of $3\Delta L$. Additional effects such as Nyquist limit [53] and the diffraction limit [54] can also be considered, but their impact is negligible for the system configuration and wavelength range used in this study.

The developed 2D ICCD-based PLIF system is validated against a conventional 0D PMT-based LIF system [48]. The comparison results are presented in section 4.1. In the PMT-based system, spatial scanning is performed by manually adjusting the focal point using a linear translation stage in 5 mm increments. The positional uncertainty is approximately 2.5 mm, as the measured positions are manually shifted post-acquisition to align with the optical focus of the ICCD-based system. The radial center, r = 0 mm, is defined as the location with the maximum fluorescence intensity in the ICCD image, based on the near-axisymmetry of the plasma. The spatial resolution of the PMT-based LIF system is determined by the iris aperture and is set to 0.9 mm for this experiment. Table 2 summarizes the spatial uncertainties of both the PMT-based and ICCD-based PLIF systems used for cross-validation.

The signatures of ion dynamics in this plasma are further analyzed by fitting the measured IVDFs to a shifted Maxwellian (Gaussian) IVDF,

$$f(v) = A_0 \exp\left(-\frac{M_i(v - v_0)^2}{2eT_i}\right) + d$$
 (1)

where A_0 is the peak intensity, M_i is the ion mass, e is the elementary charge, v_0 is the most probable velocity which also

corresponds to the mean velocity for this distribution, T_i is the ion temperature or the velocity spread in electronvolts (eV), and d is an offset constant. While multiple-Gaussian fitting functions can be employed, particularly under certain operating conditions of this plasma device [48], a single-Gaussian distribution is chosen as it provided the best fit for the experimental scenarios discussed here. The fitting procedure minimizes the chi-square (χ^2) value using the standard deviation of the measured data as the weighting input, ensuring that the resulting fit emphasizes statistically reliable data points. This fitting analysis is performed across all spatial regions of the fluorescence image to reconstruct 2D maps of ion dynamic parameters.

3.2. ICCD operating condition

The acquired images and the extracted fluorescence signals may exhibit varying levels of noise, depending not only on the metastable ion density, which is proportional to the fluorescence intensity for a given input laser power, but also on the operating conditions of the ICCD camera. Parameters such as exposure time, number of accumulations, intensifier gain, and the number of frames used for averaging can all significantly affect image quality. Consequently, the accuracy and clarity of the reconstructed IVDFs are directly influenced by the quality of the recorded images and the corresponding extracted fluorescence signals.

The quality of images obtained under different ICCD operating conditions was evaluated by repeating the measurement procedure three times and calculating the SNR of the fluorescence patterns. In this analysis, the signal is defined as the average fluorescence intensity at the brightest pixel, and the noise is the standard deviation of that intensity across three repeated measurements. Figure 3 presents the effects of two key ICCD parameters, intensifier gain, and the number of frames averaged, on the resulting SNR.

In figure 3(a), the SNR initially increases as the intensifier gain is raised, but then it decreases at higher gains due to the nonlinear amplification behavior of the intensifier. At low gain levels, both signal and noise are amplified at a similar rate. At higher gain settings, the signal amplification begins to saturate, while the noise continues to grow. This leads to a decline in SNR. This behavior suggests that using higher intensifier gain helps to highlight the peak of the IVDFs, which is useful for identifying the most probable ion velocity. However, it is less effective for accurately capturing the broadening of the distribution or ion temperature, due to increased noise.

Figure 3(b) shows the effect of the number of frames averaged. As more frames are averaged, the noise decreases, and the image quality improves. This behavior aligns with the central limit theorem, which predicts that random noise will decrease in proportion to the inverse square root of the number of samples, assuming a normal distribution. The SNR trend observed in the data qualitatively follows a square-root dependence, which supports this explanation.

For time-averaged measurements in scenario (A), the ICCD intensifier gain was set to 40 to better resolve the peak of the IVDFs. Images were obtained by averaging 15 frames, each

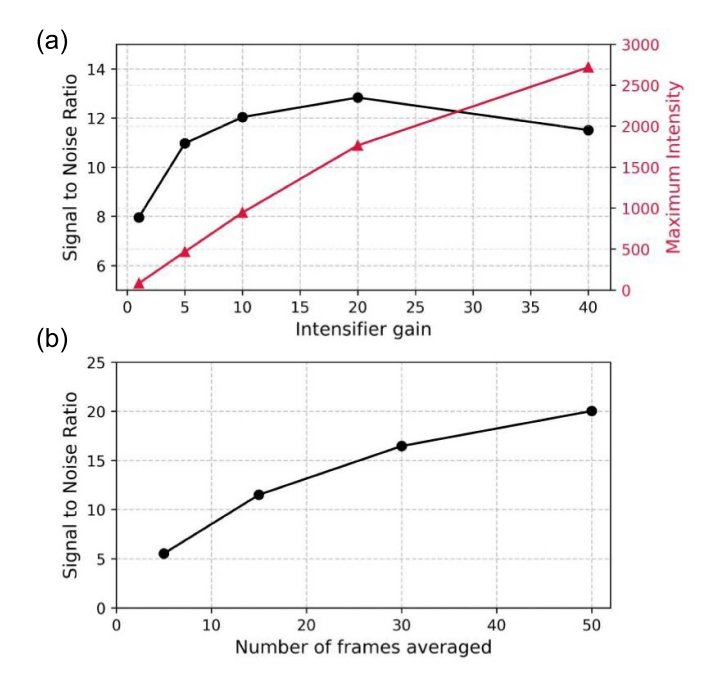


Figure 3. Effect of two ICCD acquisition parameters on image quality, quantified by the signal-to-noise ratio (SNR). The signal is defined as the maximum fluorescence intensity in the image, while noise is defined as the standard deviation of the signal across three repeated acquisitions. (a) Effect of intensifier gain, with the number of frames averaged fixed at 15. Maximum fluorescence intensity at each gain setting is also shown in red. (b) Effect of the number of frames averaged, with the intensifier gain fixed at 40. All parameter scans are conducted under the reference plasma operating condition, with the incident laser wavelength set to λ_0 .

frame captured with a 5 ms exposure accumulated 200 times, so that the total exposure time for one frame sums up to 1 s. The total time required to acquire spatially resolved IVDFs across 40 velocity points was approximately 8 min using the ICCD-based system. Notably, this duration is comparable to the time needed by the PMT-based system to measure the IVDF at a single spatial point. For time-resolved measurements in scenario (B), the exposure time was shortened to 0.2 ms, corresponding to one-tenth of the oscillation period, in order to distinguish the measured data at different timings of the plasma oscillation.

3.3. Image denoising methods

Increasing (i) the exposure time or (ii) the number of frames is an effective and straightforward way to improve image quality and obtain more reliable IVDFs. Approach (i), however, reduces the diagnostic's temporal resolution, whereas approach (ii) lengthens the total acquisition time. To address these drawbacks, it is worth considering noise filtering techniques instead of relying solely on signal accumulation.

Traditional plasma diagnostics that utilize camera-based imaging often apply standard spatial filtering methods, such as median [55, 56] or Gaussian filters [42]. These methods reduce noise by smoothing the image across the spatial domain, but

this comes at the cost of degraded spatial resolution. As a result, such techniques may not be suitable for our application, which requires accurate measurement of spatially resolved IVDFs. Since the effectiveness of denoising methods depends heavily on the structural characteristics of the image, our goal is to identify the most effective approach for processing fluorescence patterns. To this end, we quantitatively compare the performance of several image filtering techniques [57].

While operating the plasma under scenario (A) with the laser set to the central wavelength λ_0 , fluorescence images were acquired using two different ICCD configurations: one averaging over 50 frames (figure 4(a), high-SNR setup) and the other averaging over five frames (figure 4(b), low-SNR setup). As expected, the high-SNR configuration produced a clearer image, though it required ten times longer acquisition time. The objective of this analysis is to identify an effective image processing method that can denoise the low-SNR image in a way that closely approximates the high-SNR result, which is treated as the ground truth in this evaluation.

Six commonly used denoising methods were tested: singular value decomposition (SVD)-based filtering, median filtering, Gaussian filtering, Wiener filtering, bilateral filtering, and fast Fourier transform (FFT)-based low-pass filtering. Each method was applied to the low-SNR image, and the denoised results were assessed using two quantitative metrics: peak signal-to-noise ratio (PSNR) and structural similarity index measure (SSIM). Further details on each filtering technique and the calculation of quality metrics are provided in appendix B as well as [57]. The denoised images are presented in figures 4(c)–(h), and the corresponding image quality metrics are summarized in table 3.

Among the tested methods, SVD-based filtering and median filtering produced higher PSNR and SSIM values compared to the others, indicating superior denoising performance. To further evaluate their effectiveness, both methods were applied to a set of fluorescence images obtained through laser wavelength scans, as detailed in appendix B. Overall, SVD-based filtering consistently achieved better PSNR and SSIM values, unless the median filter was applied with a larger spatial window. However, increasing the window size in median filtering results in greater image blurring, which degrades the spatial resolution of the diagnostics. This tradeoff makes SVD-based filtering a more favorable choice for preserving both image quality and diagnostic resolution.

The effectiveness of each filtering method becomes more apparent when the denoised images are converted into IVDFs. Figure 5 presents IVDFs at two different spatial locations, reconstructed from images acquired using different ICCD setups and processed with various denoising methods. Additional IVDFs at other positions are provided in appendix B. At the center of the plasma, where the fluorescence signal is strong due to a higher density of metastable species, both filtering methods yield similar results. In this region, the signal-to-noise ratio is inherently high, and thus the impact of denoising is minimal. However, at the plasma periphery, where the fluorescence is weaker and the noise level is higher, the performance of SVD-based filtering becomes

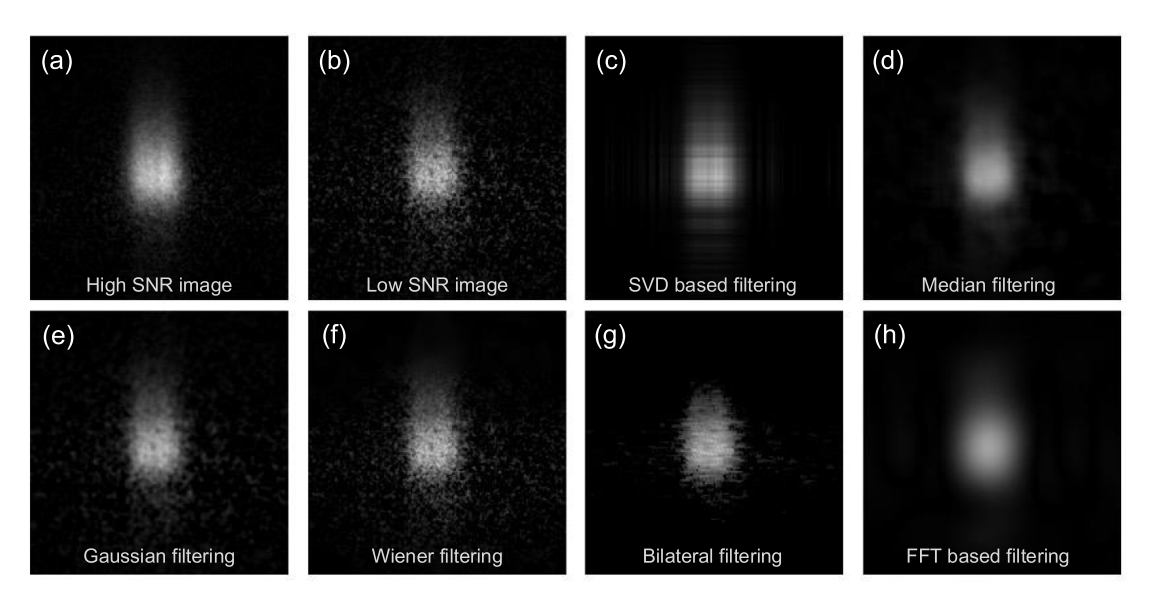


Figure 4. Fluorescence images under different ICCD operating conditions and results of various denoising methods applied to a low-SNR image. Images are cropped to zoom into the fluorescence patterns. (a) High-SNR image obtained with 50 frames averaged. (b) Low-SNR image obtained with five frames averaged. Low-SNR image denoised using the following image processing techniques: (c) SVD-based filtering, (d) Median filtering, (e) Gaussian filtering, (f) Wiener filtering, (g) Bilateral filtering, and (h) FFT-based filtering.

Table 3. PSNR and SSIM for each image denoising method applied to the low-SNR fluorescence image. The high-SNR image is used as the reference for evaluation.

	Low SNR	SVD	Median	Gaussian	Wiener	Bilateral	FFT-based
PNSR	33.7 dB	41.3 dB	40.9 dB	38.0 dB	35.5 dB	26.2 dB	34.9 dB
SSIM	0.68	0.84	0.82	0.74	0.79	0.18	0.82

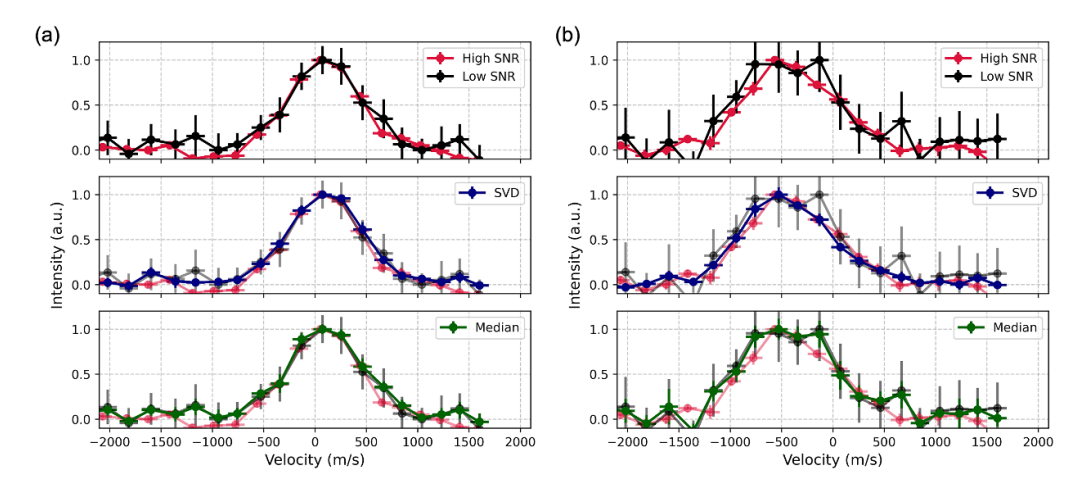


Figure 5. IVDFs at two locations: (a) r = 0 mm and (b) r = -15 mm. IVDFs are reconstructed from images acquired using the high-SNR ICCD setup (red) and the low-SNR ICCD setup (black). Denoised results from two filtering methods are also shown: SVD-based filtering retaining the most significant component (blue), and median filtering with a window size of $[51 \times 51]$ (green).

more significant. This method is effective at isolating the dominant structural features of the image from noise, allowing it to recover the underlying fluorescence pattern even under low signal conditions. As a result, the IVDFs reconstructed from SVD-denoised images more closely follow the ground truth, high-SNR curve, while also exhibiting reduced noise levels. In contrast, median filtering, while useful for general noise suppression, also blurs the finer features of the fluorescence

pattern. Hence, it fails to preserve the correct shape of the distribution. This leads to a loss of detail in the reconstructed IVDF, especially at the 'wing' region where SNR is low but contains the higher moment characteristics of IVDFs such as ion temperature.

Therefore, beyond the PSNR and SSIM metrics provided earlier, the reconstructed IVDFs further demonstrate that SVD-based filtering is more effective than median filtering for extracting fluorescence signals from noisy images. This advantage can be attributed to the selective denoising capability of SVD-based filtering, which isolates and retains the most relevant components for image reconstruction [58, 59]. In addition to its denoising performance, SVD-based filtering also preserves the spatial resolution of the measurements, as it avoids the blurring commonly introduced by conventional spatial filters, making it well-suited for spatially resolved IVDF measurements.

4. Results

4.1. Time-averaged measurements

This section presents time-averaged measurements of IVDFs obtained using the developed ICCD-based PLIF system. The validation of this diagnostic approach is discussed through a direct comparison with a conventional PMT-based LIF system. Figure 6 shows the IVDFs measured by two different LIF systems, in different radial positions of this plasma in operating scenario (A).

In each plot, the *x*-axis represents ion velocity (m s⁻¹), and the *y*-axis shows the fluorescence intensity normalized by the maximum value of the IVDF at each position to facilitate comparison. Error bars on the fluorescence intensity indicate the standard deviation from three repeated measurements. The ion velocity error bars represent a combination of the standard deviation from three measurements and the wavemeter uncertainty, which is approximately \pm 89 m s⁻¹. The radial position corresponding to each IVDF is labeled in each subplot.

Figure 7 shows the differences between IVDFs measured by each diagnostic, quantified using the cross-correlation and reduced χ^2 calculated between the two data sets.

As can be seen from the magnitude of cross-correlation, the discrepancies between the two measurements are larger at the plasma periphery than at the radial center, where the metastable density, and consequently, the fluorescence intensity and SNR are lower. As shown in figure 7(c), both diagnostics exhibit larger experimental error bars at the periphery, contributing to the observed deviations. Near r=30 mm, where the ion density is around $6\times10^9\,\mathrm{cm}^{-3}$, both diagnostics were not able to get information due to the lack of signals. Nevertheless, in the region of interest close to the bulk, both the cross-correlation and reduced χ^2 close to 1 indicates good agreement between the developed ICCD-based PLIF system and the conventional PMT-based LIF system.

Figure 8 shows the 1D radial distribution of the peak intensity (A_0) , most probable velocity (ν_0) , and the ion temperature (T_i) , extracted by fitting the IVDFs in different position to the shifted Gaussian distribution described in equation (1). The y error bars for each fitting parameters show the 95% confidence interval of the χ^2 fitting, indicating the statistical stability of the fit. The x error bars indicate the uncertainty of the spatial positions, as shown in table 1. The fitted parameter from both methods agrees with each

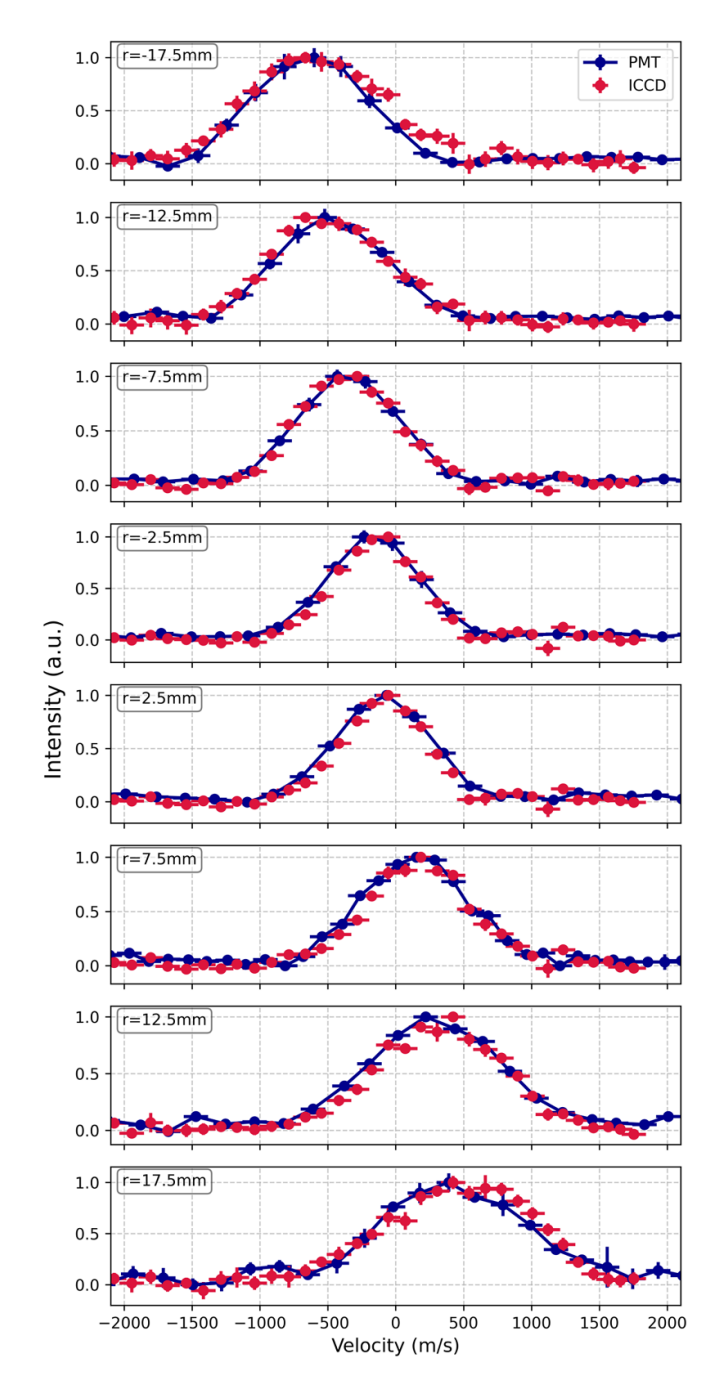


Figure 6. Comparison of IVDFs at different spatial locations, measured using PMT-based LIF (blue) and ICCD-based PLIF (red). Fluorescence intensity is normalized by the maximum value of each IVDF for visualization.

other as well as IVDFs, also supporting a successful cross-validation of the developed PLIF system against conventional measurements.

The spatially resolved characteristics of 2D IVDFs are shown in figure 9. In each contour plot, the *x*-axis and *y*-axis represent axial and radial positions, respectively. Due to the near-axisymmetry and axial uniformity of the plasma,

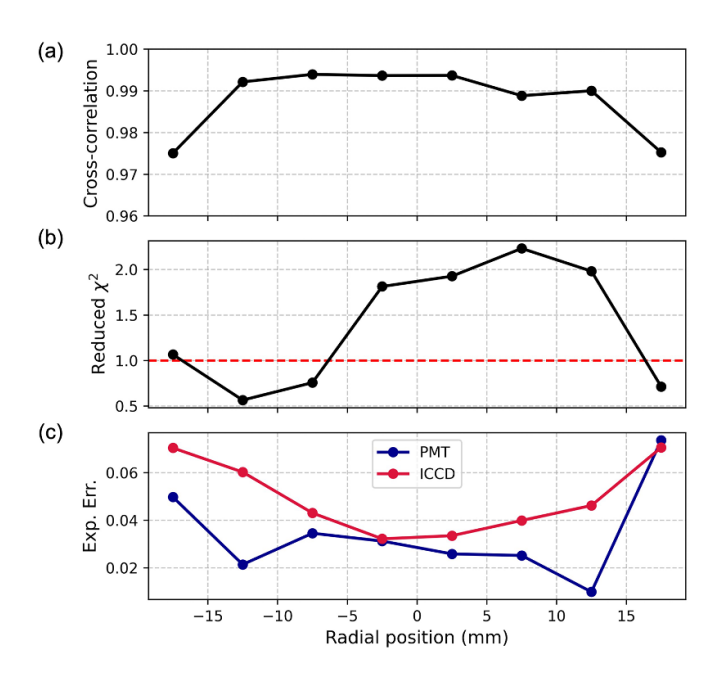


Figure 7. Quantitative comparison of measured IVDFs from PMT-based LIF and ICCD-based PLIF at different positions, using (a) cross-correlation, (b) Reduced χ^2 , and (c) the averaged experimental error bars of the IVDFs measured by each system at each position.

the fitted parameter maps exhibit radial symmetry and homogeneity along the z-direction. For visualization, only the spatial averages of the fitted parameters are shown in figure 9. It is important to note that fitting uncertainties increase toward the periphery of the plasma, where fluorescence intensity is weaker, and the SNR is lower as the plasma density decays. Consequently, some apparent spatial variations, such as the wavy structures observed in the axial direction of the ion temperature map in figure 9(c) are likely artifacts within the margin of fitting error rather than physical features.

Figure 9(a) shows the spatial map of the peak fluorescence intensity (A_0) at each position, which depends on both the local laser power and the density of ion metastables excited by the laser. The non-uniformity observed along the axial direction is primarily attributed to the spatial variation in the laser sheet's power distribution. The radial decrease in peak intensity reflects a reduction in the density of ion metastable, consistent with expectations from plasma diffusion. Figure 9(b) presents the spatial map of the most probable velocity (v_0) , which reflects the overall direction and magnitude of ion flow. The map indicates radially outward ion streaming from the plasma center, across the electric field. Ions are accelerated linearly with radial position, to the magnitude of 800 m s⁻¹ at r = 20 mm. Figure 9(c) displays the ion temperature (T_i) distribution. Near the radial center, the ion temperature is approximately 0.045 eV. Toward the plasma periphery, the ions become significantly warmer, reaching temperatures up to ~ 0.15 eV at r = 20 mm, which is more than three times higher than at the center. These spatially resolved IVDFs provide a foundation for further interpretation of ion transport and heating in this plasma source. A detailed discussion of the physical mechanisms underlying these observations is presented in section 5.

4.2. Time-resolved measurements

In this section, the applicability of this ICCD-based PLIF system on time-resolved measurements is discussed, demonstrating IVDF measurements in plasma operating scenario (B) where plasma is driven with an external oscillation applied at anticathode.

Figures 10(a)–(c) shows the time evolution of key plasma parameters in response to the oscillating anticathode potential. The plasma oscillates between two distinct operating conditions, referred to as collector and repeller modes [47, 49]. The x-axis represents time normalized by the oscillation period of 2 ms. The ICCD camera is triggered at two specific phases corresponding to each mode, as indicated by the gray and red boxes, respectively. The width of each box denotes the exposure time $\tau/10$ following the trigger signal.

The radial profiles of ion density, measured using an IP, are presented in figure 10(d). The ion density is higher in the repeller mode compared to the collector mode, as reduced axial loss of the electron beam leads to increased ionization. Notably, the ion density at the center is approximately 1.6 times greater in the repeller mode than in the collector mode. The observed variation in ion density provides a valuable test environment for evaluating the performance of the time-resolved measurements of the developed PLIF system. Previous study provides that the electron temperature and electric potential structure remains consistent between the two modes [49]. Hence, the fluorescence intensity at each mode is expected to scale proportionally with the ion density.

The IVDFs obtained from time-resolved PLIF measurements are fitted using a shifted Maxwellian distribution function. The resulting 2D maps of IVDF signatures are presented in figure 11. These time-resolved 2D maps exhibit axisymmetry, radial ion outflux and ion heating near the plasma periphery, similar to the time-averaged measurements. The corresponding 1D radial profiles at z = 0 mm are shown in figure 12. Figure 12(a) displays the peak fluorescence intensity profiles for each mode, normalized to the peak fluorescence at the radial center in the collector mode. For comparison, the ion density profiles in each mode, also normalized to the central density in the collector mode, are overlaid. The fluorescence intensity at the radial center in repeller mode is approximately 1.6 times higher than in the collector mode, consistent with ion density measurements obtained using electrostatic probe diagnostics. In each mode, the radial distribution of the peak fluorescence intensity has the same trend to the ion density profile, as expected, but exhibits a steeper gradient. This difference in slope is attributed to the center-peaked electron temperature distribution [49], which enhances fluorescence by exciting more metastable states from the same ion density. However, the ratio of fluorescence profiles and density profile at different modes align well, supporting a successful implementation of time-resolved PLIF measurements.

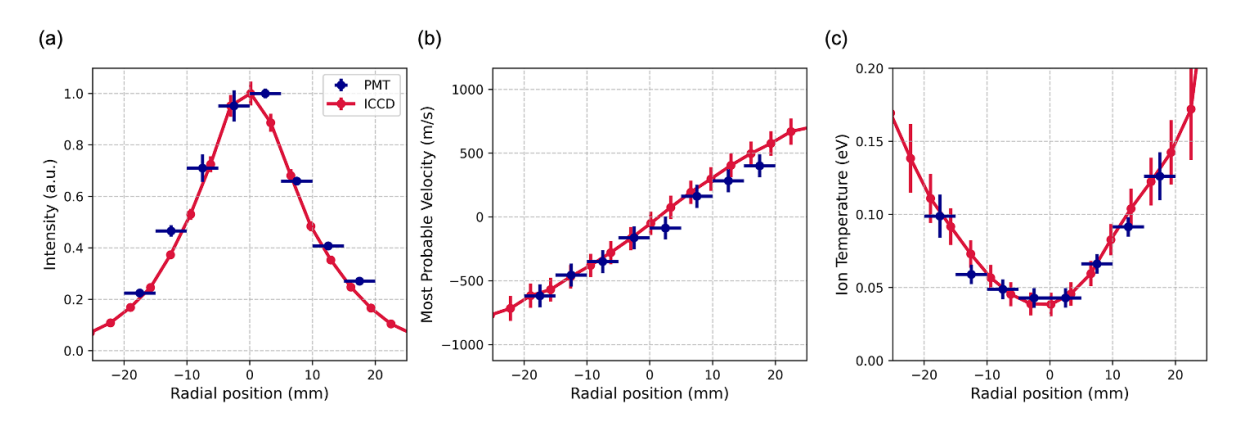


Figure 8. Radial distribution of (a) Peak fluorescence intensity, (b) most probable velocity and (c) ion temperature measured by PMT-based LIF (blue) and ICCD-based PLIF (red).

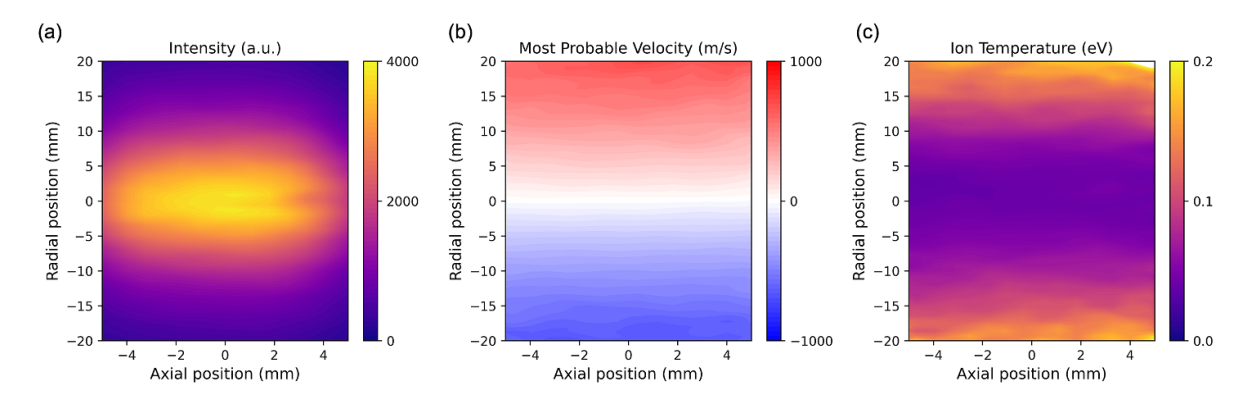


Figure 9. Experimentally obtained two-dimensional characteristics of ion dynamics, analyzed through fitting of the IVDFs. (a) Peak fluorescence intensity, (b) most probable ion velocity, (c) ion temperature.

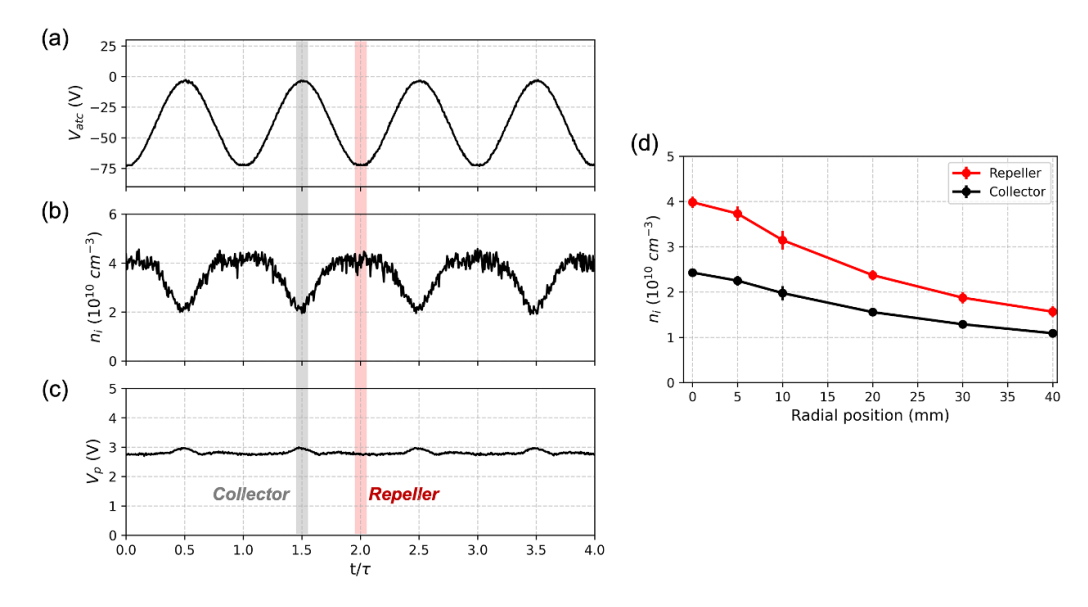


Figure 10. Time evolution of plasma parameters at the radial center, synchronized with the modulation of the anticathode potential. (a) Anticathode potential, (b) ion density, (c) plasma potential. (d) radial profiles of ion density during repeller and collector modes measured by an ion probe.

Differences in IVDF characteristics between the two modes further validate the system's time-resolving capability. For instance, the most probable ion velocity is higher in the repeller mode, linked to the enhanced plasma diffusion driven

by a steeper density gradient and a more pronounced center peak. The ion temperature profile reveals that ions are approximately twice as hot at the periphery compared to the center. This trend is similar to what was observed in scenario (A),

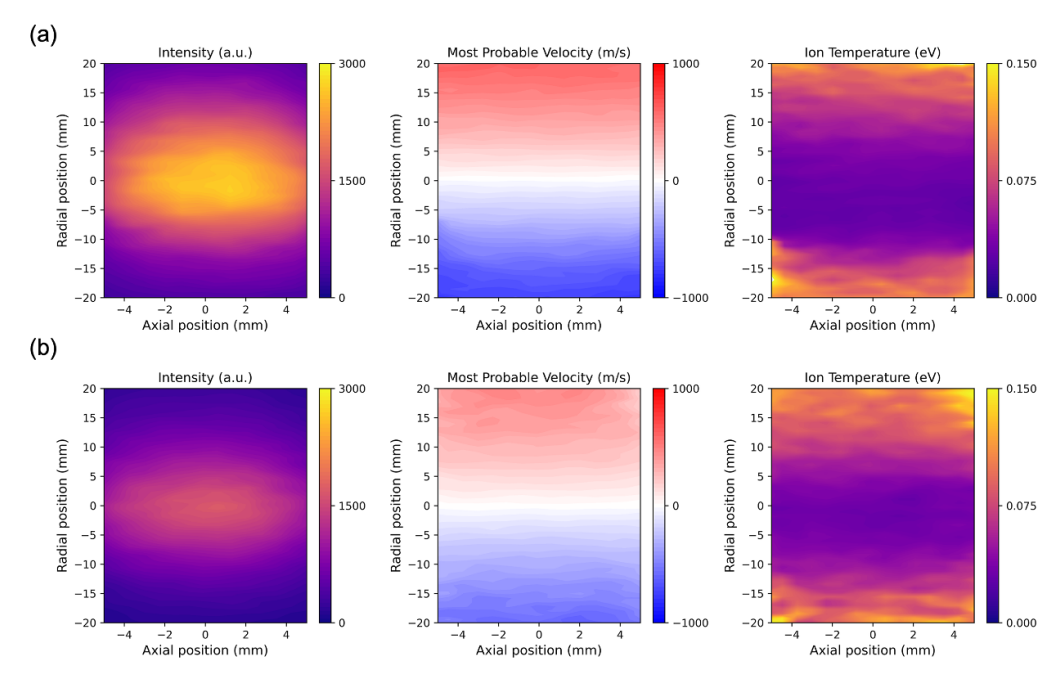


Figure 11. Experimentally obtained two-dimensional characteristics of ion dynamics, analyzed through fitting of IVDFs at two different ICCD triggering phases: (a) repeller mode, (b) collector mode. Each row displays spatial maps of peak fluorescence intensity, most probable ion velocity (m s⁻¹), and ion temperature (eV), extracted through fitting of the IVDFs in each mode.

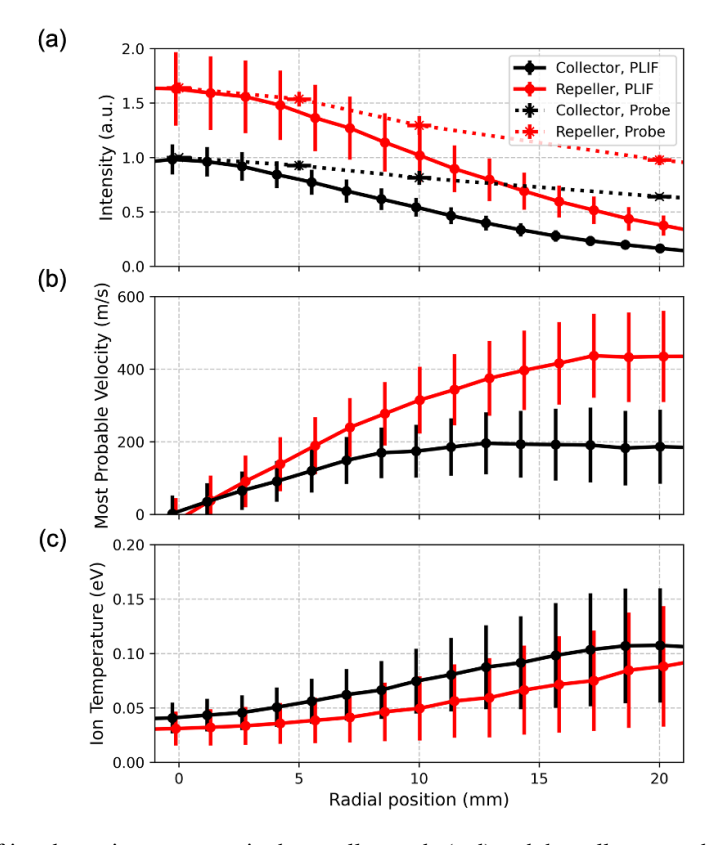


Figure 12. Radial distribution of ion dynamic parameters in the repeller mode (red) and the collector mode (black): (a) peak fluorescence intensity, with the normalized ion density profile overlaid as a dotted line, (b) most probable ion velocity, (c) ion temperature.

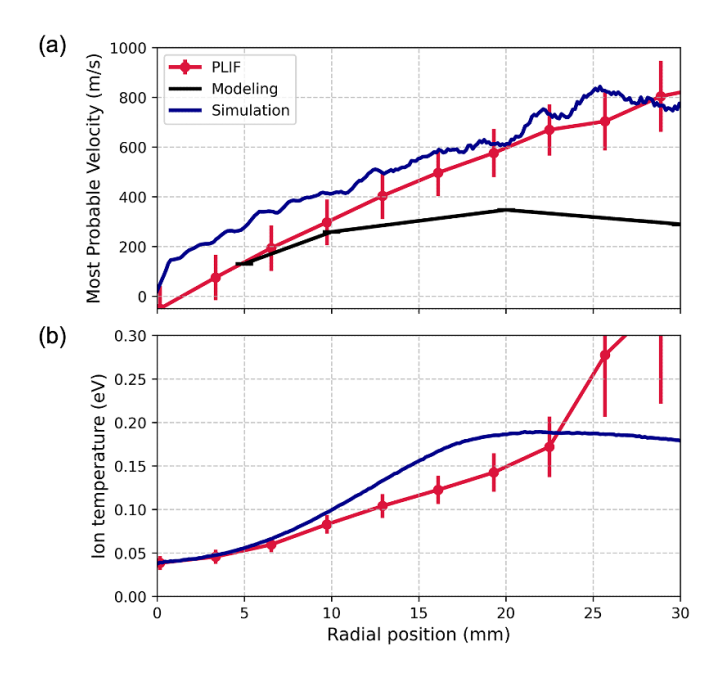


Figure 13. Radial distribution of ion dynamic parameters: (a) most probable ion velocity, (b) ion temperature. PLIF measurements (red), PIC simulation (blue) and particle balance modeling (black) are shown. The modeling and simulation results are reproduced from [50].

though to a lesser extent. Specifically, the ratio of ion temperature at r = 20 mm to the center temperature is around 2 in both modes of scenario (B), whereas it was approximately 3 in scenario (A), as discussed in section 4.1.

5. Discussions

Two robust signatures are observed from the PLIF measurements in this electron beam generated $E \times B$ plasma: (i) monotonically increasing outward-directed ion velocity, and (ii) ion heating at the plasma periphery. In this section, we further discuss on these experimental observations in comparison to 2D3V particle-in-cell (PIC) simulations tailored to this setup and particle-balance modeling detailed in [47, 50, 60, 61].

Figure 13 presents the radial profile of most probable ion velocity and ion temperature in scenario (A), both from PLIF (red) and PIC (blue). The data is extracted along the z=0 mm line of the 2D data set. The PIC simulation results are time-averaged over 418 μs once steady state is reached.

5.1. Radially outward ion flux

Figure 13(a) displays the radial profile of the most probable ion velocity. Both the PLIF measurements (red) and the PIC simulations (blue) indicate outward ion flow across the entire radius. Such a flux is expected under steady-state conditions because it compensates for volumetric ion production near the plasma center. A simplified particle balance model (black), which estimates the radial ion flux required to balance the electron beam impact ionization, and the axial ion Bohm flux calculated from the EEDF [51], also predicts an outward flux.

However, the discrepancy between the modeled velocity and the experimental or simulated values increases toward the periphery, indicating additional radial ion acceleration and loss mechanisms. To interpret this discrepancy, it is instructive to discuss the steady-state radial momentum balance equation of ions:

$$u_{\rm r}\frac{\partial u_{\rm r}}{\partial r} = \frac{e}{M_{\rm i}}\left(E_r + u_{\theta}B_z\right) + \frac{u_{\theta}^2}{r} - \frac{e}{n_{\rm i}M_{\rm i}}\frac{\partial\left(n_{\rm i}T_{\rm i}\right)}{\partial r} \tag{2}$$

where $u_{\rm r}$ and u_{θ} are the radial and azimuthal ion velocities, $n_{\rm i}$ is the ion density, E_r is the radial electric field, and B_r is the axial magnetic field. In this simplified form, ion-neutral collision drag is neglected. The left-hand side contains the convective derivative (ion inertia) term, representing radial acceleration of ions. The right-hand side comprises the driving forces: the electric field, Lorentz force, centrifugal force, and pressure gradient. Because $T_i \ll T_e$, the pressure-gradient term is negligible compared to the contribution from the electric field, which is on the order of $\sim 1 \text{ V cm}^{-1}$. In contrast, the coupling of azimuthal rotation into the radial direction can be significant. For example, a prior study simulating Penning E × B discharges found that the centrifugal force can balance the inward-directed electric field in steady state [60]. Although the origin of azimuthal ion rotation in this partially magnetized plasma remains uncertain, potential contributors include ion rotation associated with magnetization [62] and interactions with azimuthally rotating spoke structures. Furthermore, within this fluid framework, the role of kinetic effects, such as the coupling of ion motion to plasma wave and instabilities, cannot be fully captured. A detailed quantitative assessment of these effects is left for future work.

5.2. Ion heating at the plasma periphery

Figure 13(b) shows the radial profile of the ion temperature from the radial velocity spread. While the core ion temperature remains close to the room-temperature background gas $(T_g \sim 0.03 \text{ eV})$ [48], PLIF measurements (red) reveal a pronounced peripheral ion temperature increase to 0.15-0.2 eV. Earlier single-point LIF studies provided preliminary evidence of warm ion production in this device [48], but the this work offers the first detailed radial map. The PIC simulation (blue) also predicts the formation of warm ions, consistent with the magnitude and radial location of the heating measured by PLIF. The observed peripheral ion heating coincides with the region where an azimuthally rotating spoke is observed at $r \approx 15$ mm [10]. Recent theoretical studies on $E \times B$ plasmas, support the interpretation that the spoke instability is responsible for this peripheral ion heating [60, 61]. The spoke can act as a moving potential structure that traps and energizes ions: as the spoke rotates azimuthally, ions are accelerated by the time-varying azimuthal E_{θ} fields and can gain kinetic energy. Time-resolved PLIF carried out under the higherpressure scenario (B) further supports this picture. The elevated neutral density damps spoke activity [10], which may reduce spoke-driven heating [58, 59] and lowers the edge temperature rise to roughly a factor of two, considerably weaker than in scenario (A). Nevertheless, a quantitative discrepancy

between PIC and PLIF remains. The simulation predicts temperature saturation, whereas PLIF shows a monotonic rise. This could be artifacts of the simulation boundary condition [61]. The computational domain is set half the vessel radius used in the experiment for computational efficiency, where this could suppress the growth of rotating spoke amplitude before it fully develops.

6. Conclusion

In this work, we developed and implemented a PLIF diagnostic based on a compact, low-power CW TDL for spatiotemporally resolved IVDF measurements in an electron beam generated $E \times B$ plasma. This ICCD-based PLIF system, optimized through a systematic evaluation of camera operating parameters and image denoising techniques, enables high-fidelity measurements while significantly reducing acquisition time compared to a conventional PMT-based, mechanically scanned LIF system. By capturing the entire spatial distribution in the time required for a single-point PMT measurement, the PLIF system makes it feasible to investigate transient and spatially complex plasma behavior in detail.

The enhanced capability of the diagnostic directly enabled the first 2D maps of IVDFs in this source, revealing key ion dynamic signatures: (i) an outward-directed ion flux propagating across the inward electric field, and (ii) pronounced peripheral ion heating, with ion temperatures at the edge reaching approximately three times the core value. These observations, validated against kinetic simulations, suggest additional particle loss mechanisms beyond those captured by particle-balance modeling that may link to the anomalous azimuthal rotation of ions. The warm-ion population detected at the periphery provides experimental support for theories linking ion heating to rotating spoke instabilities, thereby connecting the diagnostic observations to fundamental instability physics in $E \times B$ plasmas. The timeresolving capability of the PLIF system further enabled the capture of dynamic oscillations between distinct plasma operating modes, with fluorescence-based density maps in close agreement with probe measurements. This capability opens a pathway to studying ion kinetics under temporally modulated conditions, such as pulsed biasing or spoke-driven fluctuations.

Looking forward, the combination of simplified setup, high spatial coverage, and temporal resolving capability makes this PLIF system a powerful tool for investigating ion dynamics in various low-temperature plasmas. Further improvements of system are encouraged, including integration of advanced imaging devices such as electron-multiplying ICCDs or machine learning based image denoising filters. With improved temporal resolution and sensitivity, this system is expected to extend to a wider range of low-temperature plasmas, supporting future advances in plasma physics and the development of next-generation plasma sources.

Data availability statement

All data that support the findings of this study are included within the article (and any supplementary files).

Acknowledgments

This research was supported by the U.S. Department of Energy, Office of Fusion Energy Sciences, under Contract No. DE-AC02-09CH11466, as a part of the Princeton Collaborative Low Temperature Plasma Research Facility (PCRF). The authors thank Dr Shurik Yatom for fruitful discussions on PLIF and Timothy K. Bennett for his technical support with the electron beam chamber. The authors also thank Ms. Mina Papahn Zadeh, Mr. Mikhail Tyushev, and Professor Andrei Smolyakov of the University of Saskatchewan for providing the PIC simulation data used in comparison with the experimental results.

Appendix A. Discussion on the background subtraction

The proposed ICCD-based PLIF system is more tolerant on plasma drift on longer time scale compared to the conventional LIF system, as mentioned in section 3.2. However, it is worth to discuss further about the criticality of this assumption on the further possible application of this system to different plasma sources. We assume that the background emission from the plasma remains sufficiently stable over time, such that its drift or fluctuation is smaller than the LIF. This allows a single background image to be used for all fluorescence images acquired at different laser wavelengths and at different times. If, however, the background emission fluctuates rapidly and more strongly than the fluorescence signal, inaccurate background subtraction may lead to failure in proper extraction of the fluorescence. The residual floor in reconstructed IVDFs attributed to the improper subtraction will artifact the fitting as well [42].

To evaluate the reliability of the above assumption in our plasma source, additional measurements were conducted under scenario (A). Using a mechanical chopper as the trigger for the ICCD camera, one image with laser incidence and one background image without laser incidence were recorded at each laser wavelength during the scan, separated by a 10 ms interval. This short delay allows the two images to be considered as captured at the same macroscopic time scale. Figure 14 presents the deviation of the maximum intensity in the background images and the maximum intensity of the extracted fluorescence images throughout the scan. The scan sequence is indicated by an arrow, and the entire process took approximately 8 min, comparable to the duration required for a single-point measurement using the conventional LIF method. The results show that the variation in background signal is orders of magnitude smaller than the fluorescence signal

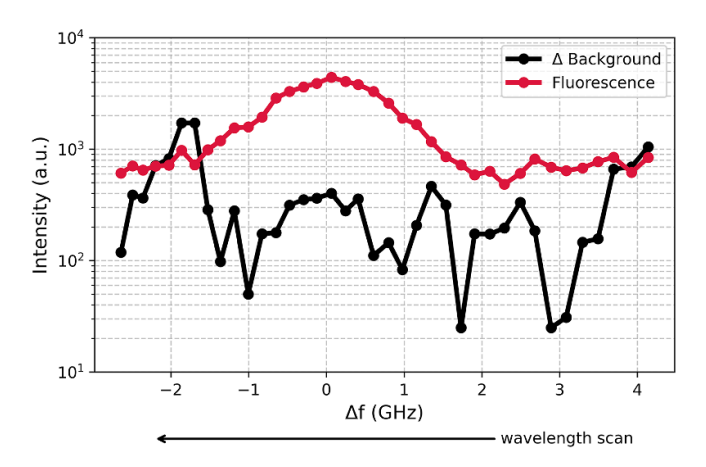


Figure 14. Log-scale plot of the intensity drift in the background image and the maximum intensity of the extracted fluorescence image during the laser wavelength (frequency) scan.

within the wavelength range where the peak and broadening of the IVDFs are primarily resolved. However, at the tail of the scan (e.g. around $\Delta f = 2$ GHz), background deviations can exceed the fluorescence signal if the latter is weak. Therefore, for broader implementation of the proposed PLIF system in different plasma sources, it is essential to quantify background drift or fluctuation relative to the fluorescence signal to assess the system's feasibility.

Appendix B. Details on the image denoising methods

In this section, we detail the analysis of image denoising results introduced in section 3.3. Six denoising methods are applied to the low-SNR image (figure 4(b)) and compared against the high-SNR reference image (figure 4(a)) using two quantitative metrics: PSNR and SSIM [57].

PSNR evaluates the fidelity of a denoised image by calculating the ratio between the maximum possible pixel intensity and the mean squared error between the denoised image and the reference. Higher PSNR values indicate better denoising performance, as they correspond to a smaller deviation from the ground truth. However, PSNR is based solely on pixelwise intensity differences and may not fully capture perceived image quality.

SSIM, in contrast, assesses the perceptual similarity between images by incorporating structural information, luminance, and contrast. It produces values ranging from -1 to 1, with 1 indicating perfect structural similarity. Because it captures texture and structural content, SSIM is more aligned with human visual perception and is therefore often more appropriate for evaluating denoised image quality.

The six denoising methods evaluated are: SVD-based filtering, median filtering, Gaussian filtering, Wiener filtering, bilateral filtering, and FFT-based filtering. The working principle and the filtering parameters of each filter is introduced below.

SVD-based filtering works by decomposing the image into singular values and corresponding singular vectors, enabling noise suppression through the selective retention of dominant components. This method is effective in enhancing image quality by preserving essential structures while removing noise. The number of retained components is varied from 1 to 3 to find the optimal filtering parameter. For instance, 'SVD, 2nd' in this analysis refers to retaining only the first and second most significant components, while discarding the rest assumed to contain noise.

Median filtering is a nonlinear filtering technique that replaces each pixel value with the median of the intensities in its neighborhood window $[N \times N]$, effectively removing impulsive noise. It is particularly effective in suppressing saltand-pepper noise due to its ability to reject outliers. The window size is varied from 11 to 51 to find the optimal filtering parameter.

Gaussian filtering applies a convolution operation with a Gaussian kernel, providing smooth image results by reducing high-frequency noise components. It achieves noise suppression through weighted averaging, where pixels closer to the center have higher weights, ensuring minimal distortion of the image details. The width of the Gaussian kernel σ is varied from 1 to 3.

Wiener filtering is a linear filtering technique that minimizes the mean square error between the estimated and true signal, under the assumption of a stationary signal and noise process. It adapts to local image variance, providing stronger noise suppression in high-SNR regions while preserving important image features. The primary tuning parameter is the size of the local neighborhood window $[N \times N]$, which determines the area over which local statistics (mean and variance) are computed for adaptive filtering. The size of the local window is scanned over the range 11-51.

Bilateral filtering preserves edges while reducing noise by considering both spatial proximity and intensity similarity when averaging pixel values. It applies a weighted average, where the weights are determined by two Gaussian functions: one based on geometric closeness (spatial domain) and the

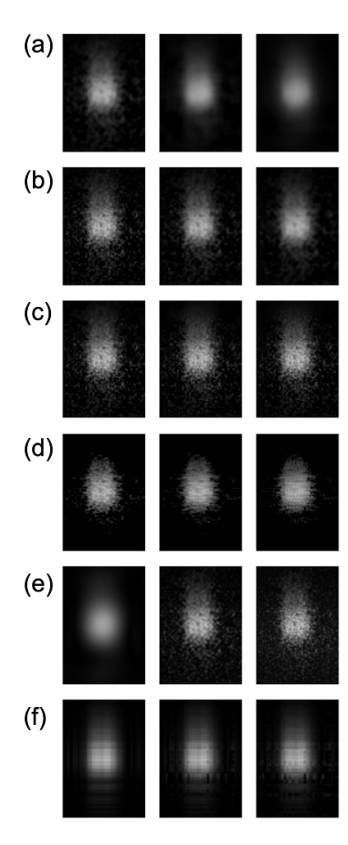


Figure 15. Low-SNR denoising results of the fluorescence image at the laser frequency of $\Delta f = 0$, using various filtering parameters. Rows correspond to different methods, and columns within each row illustrate changes in image quality when different denoising parameters are applied. (a) Median filtering with window sizes of 11, 25, and 51. (b) Gaussian filtering with $\sigma = 1$, 2, and 3. (c) Wiener filtering with window sizes of 11, 25, and 51. (d) Bilateral filtering with $\sigma = 1$, 2, and 3. (e) FFT-based low-pass filtering with cutoffs of 0.01, 0.1, and 0.5. (f) SVD-based filtering retaining up to ranks 1, 2, and 3.

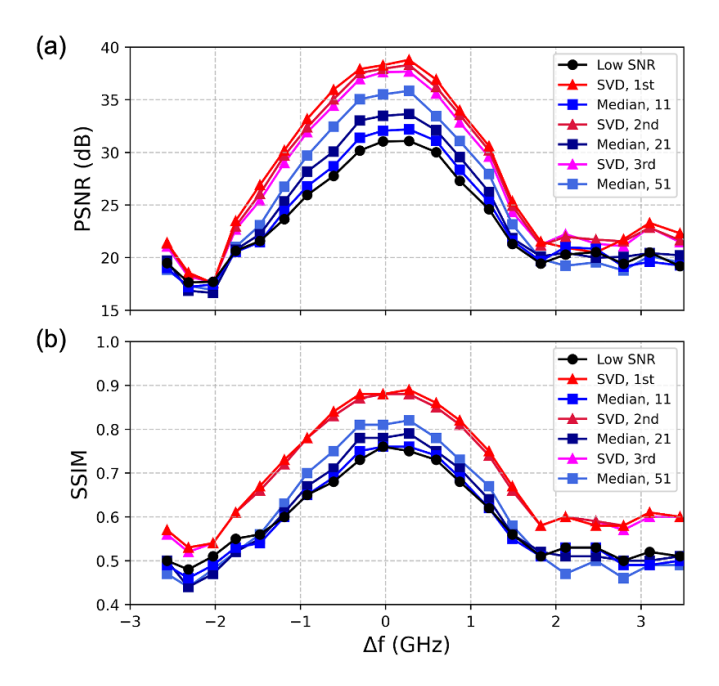


Figure 16. Quantitative evaluation of denoising performance across laser wavelength (frequency) scan Δf using (a) PSNR and (b) SSIM metrics. Results are shown for fluorescence images reconstructed using SVD-based filtering and Median filtering. Labels such as 'SVD, 2nd,' indicate SVD-based filtering including components up to the 2nd significance. Labels such as 'Median, 21' refer to median filtering applied with a [21 \times 21] square window.

other on photometric similarity (intensity domain). The degree of smoothing is controlled by two parameters, σ_s for spatial distance and σ_r for intensity difference. Smaller σ values result in stronger edge preservation, while larger values lead to more aggressive smoothing. It is widely used for denoising and edge-preserving smoothing in computer vision and image processing tasks. In this study, the spatial variance σ_s is scanned over the range $\sigma_s = 1$ to 3.

FFT based filtering operates in the frequency domain by transforming the image, filtering out high-frequency components associated with noise, and then performing an inverse transform to reconstruct the denoised image. This approach allows selective attenuation of noise frequencies while preserving important structural components. FFT-based filtering is particularly effective for periodic noise removal and signal processing applications. Here, the high-frequency cutoff is varied from 0.01 to 0.5 to find the optimal setting.

The resulting denoised images with different parameters are shown in figure 15, while the result with the highest PSNR and SSIM for each method is displayed in figure 4. As summarized in section 3.3, SVD-based filtering gave the best denoising results.

Figure 16 shows the PSNR and SSIM in different laser wavelength, which gives differently patterned fluorescence images. Overall, the SVD-based filtering gives better PSNR and SSIM unless median filter uses a larger window of filtering so that the image is more blurred, and we lose the spatial resolution. On the other hand, the above plot shows that retaining one component from the SVD-based filtering gives the best PSNR, which indicates that the most significant (1st) component contains the fluorescence structure, while components lower than 2nd significance contains noise. Therefore, selecting only the first component in SVD-based filtering is sufficient for effective denoising across all laser wavelengths used to reconstruct the IVDFs.

ORCID iDs

References

- [1] Lee D, Hershkowitz N and Severn G D 2007 Measurements of Ar⁺ and Xe⁺ velocities near the sheath boundary of Ar–Xe plasma using two diode lasers Appl. Phys. Lett. 91 041505
- [2] Lee D, Oksuz L and Hershkowitz N 2007 Exact solution for the generalized Bohm criterion in a two-ion-species plasma *Phys. Rev. Lett.* 99 155004
- [3] Yip C-S, Hershkowitz N and Severn G 2010 Experimental test of instability-enhanced collisional friction for determining ion loss in two ion species plasmas *Phys. Rev. Lett.* 104 225003
- [4] Hershkowitz N, Yip C-S and Severn G D 2011 Experimental test of instability enhanced collisional friction for determining ion loss in two ion species plasmas *Phys. Plasmas* 18 057102
- [5] Moore N B, Gekelman W and Pribyl P 2016 Ion energy distribution function measurements by laser-induced

- fluorescence in a dual radio frequency sheath *J. Vac. Sci. Technol. A* **34** 021303
- [6] Baalrud S D, Scheiner B, Yee B T, Hopkins M M and Barnat E 2020 Interaction of biased electrodes and plasmas: sheaths, double layers, and fireballs *Plasma Sources Sci. Technol.* 29 053001
- [7] Jacobs B, Gekelman W, Pribyl P and Barnes M 2010 Phase-resolved measurements of ion velocity in a radio-frequency sheath *Phys. Rev. Lett.* 105 075001
- [8] Britun N, Konstantinidis S and Snyders R 2015 An overview on time-resolved optical analysis of HiPIMS discharge Plasma Process. Polym. 12 1010–27
- [9] Versolato O, Kaganovich I, Bera K, Lill T, Lee H-C, Hoekstra R, Sheil J and Nam S K 2024 Plasma sources for advanced semiconductor applications *Appl. Phys. Lett.* 125 230401
- [10] Chopra N S and Raitses Y 2025 Anticathode effect on multimodal azimuthal oscillations in electron beam generated E×B plasma Appl. Phys. Lett. 126 064101
- [11] Romadanov I, Raitses Y, Diallo A, Kaganovich I D, Kentaro H and Andrei S 2017 Time-resolved measurements of modulated breathing oscillations in cylindrical Hall thruster *Proc.*, *Int. Electric Propulsion Conf.*
- [12] Janhunen S, Smolyakov A, Chapurin O, Sydorenko D, Kaganovich I and Raitses Y 2018 Nonlinear structures and anomalous transport in partially magnetized E×B plasmas Phys. Plasmas 25 011608
- [13] Koshkarov O, Smolyakov A, Raitses Y and Kaganovich I 2019 Self-organization, structures, and anomalous transport in turbulent partially magnetized plasmas with crossed electric and magnetic fields *Phys. Rev. Lett.* 122 185001
- [14] Kaganovich I D et al 2020 Physics of E × B discharges relevant to plasma propulsion and similar technologies Phys. Plasmas 27 120601
- [15] Kim J Y, Jang J Y, Choi J, Wang J, Jeong W I, Elgarhy M A I, Go G, Chung K-J and Hwang Y S 2021 Magnetic confinement and instability in partially magnetized plasma Plasma Sources Sci. Technol. 30 025011
- [16] Choi J, Cheon C, Hwang Y S, Chung K-J and Kim J Y 2023 Rotating spoke frequency in E × B penning source with two-ion-species plasma *Plasma Sources Sci. Technol.* 32 01LT01
- [17] Lee M, Cheon C, Choi J, Lee H J, Hwang Y S, Chung K-J and Kim J Y 2023 Azimuthal and axial dispersion relations of low-frequency oscillations in partially magnetized plasma with crossed electric and magnetic fields *Phys. Plasmas* 30 103502
- [18] Kim J Y, Chung K-J, Takahashi K, Merino M and Ahedo E 2023 Kinetic electron cooling in magnetic nozzles: experiments and modeling *Plasma Sources Sci. Technol.* 32 073001
- [19] Scime E, Biloiu C, Compton C, Doss F, Venture D, Heard J, Choueiri E and Spektor R 2005 Laser induced fluorescence in a pulsed argon plasma Rev. Sci. Instrum. 76 026107
- [20] Gahan D, Daniels S, Hayden C, Scullin P, O'Sullivan D, Pei Y T and Hopkins M B 2012 Ion energy distribution measurements in RF and pulsed dc plasma discharges *Plasma Sources Sci. Technol.* 21 024004
- [21] Economou D J 2014 Pulsed plasma etching for semiconductor manufacturing J. Phys. D: Appl. Phys. 47 303001
- [22] Wen D-Q, Zhang Q-Z, Jiang W, Song Y-H, Bogaerts A and Wang Y-N 2014 Phase modulation in pulsed dual-frequency capacitively coupled plasmas J. Appl. Phys. 115 233303
- [23] Han J, Pribyl P, Gekelman W and Paterson A 2020 Three-dimensional measurements of fundamental plasma parameters in pulsed ICP operation *Phys. Plasmas* 27 063509

- [24] Baloniak T, Reuter R and Von Keudell A 2010 Fundamental aspects of substrate biasing: ion velocity distributions and nonlinear effects J. Phys. D: Appl. Phys. 43 335201
- [25] Lafleur T and Booth J P 2012 Control of the ion flux and ion energy in CCP discharges using non-sinusoidal voltage waveforms J. Phys. D: Appl. Phys. 45 395203
- [26] Krüger F, Wilczek S, Mussenbrock T and Schulze J 2019 Voltage waveform tailoring in radio frequency plasmas for surface charge neutralization inside etch trenches *Plasma* Sources Sci. Technol. 28 075017
- [27] Severn G D, Edrich D A and McWilliams R 1998 Argon ion laser-induced fluorescence with diode lasers Rev. Sci. Instrum. 69 10–15
- [28] Mazouffre S 2012 Laser-induced fluorescence diagnostics of the cross-field discharge of Hall thrusters *Plasma Sources* Sci. Technol. 22 013001
- [29] Yip C-S and Jiang D 2021 Laser induced fluorescence diagnostic for velocity distribution functions: applications, physics, methods and developments *Plasma Sci. Technol.* 23 055501
- [30] Romadanov I and Raitses Y 2023 A confocal laser-induced fluorescence diagnostic with an annular laser beam Rev. Sci. Instrum. 94 073002
- [31] Romadanov I, Raitses Y and Smolyakov A 2024 Wavelength modulation laser-induced fluorescence for plasma characterization Rev. Sci. Instrum. 95 073516
- [32] Dale E T 2019 Investigation of the Hall Thruster Breathing Mode (University of Michigan)
- [33] Kirkwood D M *et al* 2018 Frontiers in thermionic cathode research *IEEE Trans. Electron. Devices* **65** 2061–71
- [34] Cunge G, Pelissier B, Joubert O, Ramos R and Maurice C 2005 New chamber walls conditioning and cleaning strategies to improve the stability of plasma processes *Plasma Sources Sci. Technol.* 14 599–609
- [35] Raitses Y, Staack D, Smirnov A and Fisch N J 2005 Space charge saturated sheath regime and electron temperature saturation in Hall thrusters *Phys. Plasmas* 12 073507
- [36] Romadanov I, Raitses Y, Diallo A, Hara K, Kaganovich I D and Smolyakov A 2018 On limitations of laser-induced fluorescence diagnostics for xenon ion velocity distribution function measurements in Hall thrusters *Phys. Plasmas* 25 033501
- [37] Wang S and Hanson R K 2019 Quantitative 2-D OH thermometry using spectrally resolved planar laser-induced fluorescence Opt. Lett. 44 578
- [38] Dorst R S, Constantin C G, Schaeffer D B, Pilgram J J and Niemann C 2022 Planar laser induced fluorescence mapping of a carbon laser produced plasma Rev. Sci. Instrum. 93 103518
- [39] Stopper U, Lindner P and Schumacher U 2007 Three-dimensional analysis of microwave generated plasmas with extended planar laser-induced fluorescence Rev. Sci. Instrum. 78 043508
- [40] Jacobs B, Gekelman W, Pribyl P, Barnes M and Kilgore M 2007 Laser-induced fluorescence measurements in an inductively coupled plasma reactor *Appl. Phys. Lett.* 91 161505
- [41] Lee H, Kim N-K, Lee M-G, Kwon J-W, Son S H, Bae N, Park T, Park S and Kim G-H 2022 Investigation of ion collision effect on electrostatic sheath formation in weakly ionized and weakly collisional plasma *Plasma Sources Sci. Technol.* 31 084006
- [42] Paul M C and Scime E E 2021 Continuous-wave planar laser induced fluorescence with a fast camera *Rev. Sci. Instrum.* **92** 043532

- [43] Shi P and Scime E E 2023 Multi-dimensional incoherent Thomson scattering system in PHAse Space MApping (PHASMA) facility Rev. Sci. Instrum. 94 023501
- [44] Lieberman M A and Allan J L 2005 Principles of Plasma Discharges and Materials Processing (Wiley)
- [45] Chabert P and Nicholas B 2011 *Physics of Radio-frequency Plasmas* (Cambridge University Press)
- [46] Yatom S, Chopra N, Kondeti S, Petrova T B, Raitses Y, Boris D R, Johnson M J and Walton S G 2023 Measurement and reduction of Ar metastable densities by nitrogen admixing in electron beam-generated plasmas *Plasma* Sources Sci. Technol. 32 115005
- [47] Chopra N 2025 Boundary-induced Kinetic Effects in Low Temperature E × B Plasmas (Princeton University)
- [48] Chopra N S, Romadanov I and Raitses Y 2024 Production of warm ions in electron beam generated E × B plasma Appl. Phys. Lett. 124 064101
- [49] Chopra N S, Romadanov I and Raitses Y 2024 Anticathode effect on electron kinetics in electron beam generated E × B plasma Plasma Sources Sci. Technol. 33 125003
- [50] Chopra N S, Zadeh M P, Tyushev M, Smolyakov A, Likhanskii A and Raitses Y 2025 Multimodal azimuthal oscillations in electron beam generated E×B plasma *Phys. Plasmas* 32 073511
- [51] Kondeti V S S K, Yatom S, Romadanov I, Raitses Y, Dorf L and Khomenko A 2024 Report on laser-induced fluorescence transitions relevant for the microelectronics industry and sustainability applications J Vac. Sci. Technol. A 42 063005
- [52] Young C V, Fabris A L, MacDonald-Tenenbaum N A, Hargus W A and Cappelli M A 2018 Time-resolved laser-induced fluorescence diagnostics for electric propulsion and their application to breathing mode dynamics *Plasma Sources Sci. Technol.* 27 094004
- [53] Ruderman D L and Bialek W 1992 Seeing beyond the Nyquist limit Neural Comput. 4 682–90
- [54] Shahram M and Milanfar P 2004 Imaging below the diffraction limit: a statistical analysis *IEEE Trans. Image Process.* 13 677–89
- [55] Ding C-P, Peterson B, Schmidt M, Dreizler A and Böhm B 2019 Flame/flow dynamics at the piston surface of an IC engine measured by high-speed PLIF and PTV *Proc. Combust. Inst.* 37 4973–81
- [56] Li T, Lian T, Huang B, Yang X, Liu X and Li Y 2021 Liquid film thickness measurements on a plate based on brightness curve analysis with acute PLIF method *Int. J. Multiph. Flow* 136 103549
- [57] Fan L, Zhang F, Fan H and Zhang C 2019 Brief review of image denoising techniques Vis. Comput. Ind. Biomed. Art 2 7
- [58] Malini S and Moni R S 2015 Image denoising using multiresolution singular value decomposition transform *Proc. Comput. Sci.* 46 1708–15
- [59] Walton J and Fairley N 2005 Noise reduction in x-ray photoelectron spectromicroscopy by a singular value decomposition sorting procedure J. Electron Spectrosc. Relat. Phenom. 148 29–40
- [60] Tyushev M, Papahn Zadeh M, Chopra N S, Raitses Y, Romadanov I, Likhanskii A, Fubiani G, Garrigues L, Groenewald R and Smolyakov A 2025 Mode transitions and spoke structures in E×B Penning discharge *Phys. Plasmas* 32 013511
- [61] Tyushev M, Papahn Zadeh M, Sharma V, Sengupta M, Raitses Y, Boeuf J-P and Smolyakov A 2023 Azimuthal structures and turbulent transport in Penning discharge Phys. Plasmas 30 033506
- [62] Gueroult R, Rax J M and Fisch N J 2017 Centrifugal instability in the regime of fast rotation *Phys. Plasmas* 24 082102